A Combined Magnetic-Acoustic Device for Simultaneous, Coaligned Application of Magnetic and Ultrasonic Fields

Lester C. Barnsley, Michael D. Gray, Estelle Beguin, Dario Carugo, and Eleanor Stride*

Acoustically-responsive microbubbles have been widely researched as agents for both diagnostic and therapeutic applications of ultrasound. There has also been considerable interest in magnetically-functionalised microbubbles as multi-modality imaging agents and carriers for targeted drug delivery. In this paper, we present a design for an integrated device capable of generating co-aligned magnetic and acoustic fields in order to accumulate microbubbles at a specific location and to activate them acoustically. For this proof-of-concept study, the device was designed to concentrate microbubbles at a distance of 10 mm from the probe's surface, commensurate with relevant tissue depths in preclinical small animal models. Previous studies have indicated that both microbubble concentration and duration of cavitation activity are positively correlated with therapeutic effect. The utility of the device was assessed in vitro tests in a tissue-mimicking phantom containing a single vessel (1.2 mm diameter). At a peak fluid velocity of 4.2 mm s^{-1} microbubble accumulation was observed under B-mode ultrasound imaging and the corresponding cavitation activity was sustained for a period more than 4 times longer than that achieved with an identical acoustic field but in the absence of a magnet. The feasibility of developing a larger scale device for human applications is discussed.

1. Introduction

Whilst the concept of magnetic drug targeting (MDT) is more than fifty years old,[1] the development of magnetically respon-

Dr. L. C. Barnsley, Dr. M. D. Gray, E. Beguin, Dr. D. Carugo,
Prof. E. Stride
Institute of Biomedical Engineering
Department of Engineering Science
University of Oxford
Oxford OX3 7DQ, UK
E-mail: eleanor.stride@eng.ox.ac.uk
Dr. L. C. Barnsley
Jülich Centre for Neutron Science at Heinz Maier-Leibnitz Zentrum
Forschungszentrum Jülich GmbH
85748 Garching, Germany
Dr. D. Carugo
Faculty of Engineering and the Environment
University of Southampton
Southampton SO17 1BJ, UK

The ORCID identification number(s) for the author(s) of this article can be found under https://doi.org/10.1002/admt.201800081.

sive therapeutic particles has received renewed interest with the advent of super-paramagnetic iron oxide nanoparticles (SPIONs), which can be actuated by external magnetic field sources to localize and concentrate therapeutic agents in a target region. MDT is seen as a promising means of improving the effectiveness of therapy noninvasively and reducing the risk of toxic side effects associated with systemic administration.[2] However, there are a number of challenges to address before the technique can be considered clinically viable.[3] Carrier formulations need to be optimized,[4–6] and it is increasingly apparent that the magnet must be designed to generate a sufficient magnetic force over the target region to capture a therapeutically relevant quantity of carrier particles from the circulatory system.[7–9] Additionally, the presence of strong magnetic forces during MDT can complicate the use of some imaging modalities, particularly magnetic resonance imaging (MRI), making it difficult to gather reliable information regarding the effectiveness of a treatment protocol during therapy.[10–12]

Ultrasound is a widely used imaging modality that is highly compatible with magnetic targeting, as there is negligible direct interaction between acoustic and magnetic fields in biological systems. Microbubbles have been used clinically for decades as an ultrasound contrast agent due to their strong, nonlinear response to acoustic fields.[13,14] Additionally, microbubbles can be formulated to carry bioactive molecules,[15,16] and utilized for localized drug delivery by exploiting their ability to cavitate under ultrasound exposure to promote drug transport and cellular uptake.[16–19] Several recent studies have explored the possibility of increasing treatment localization through magnetic targeting by incorporating SPIONs into the microbubble coating.[5,20–23] It has been shown in multiple in vitro and in vivo studies that there is a positive correlation between therapeutic effect and both the level and duration of cavitation activity.[24–26] Hence it is desirable to apply both magnetic and ultrasound fields simultaneously to a target region to maintain a high concentration of microbubbles throughout the treatment. In simple in vitro experiments this can be achieved relatively easily[5] but in more complex models and in vivo this is often challenging due to space constraints.[27]

In this paper, we present the design and assembly of a combined magnetic-acoustic device (MAD) for the simultaneous application of coaligned magnetic and acoustic fields to both
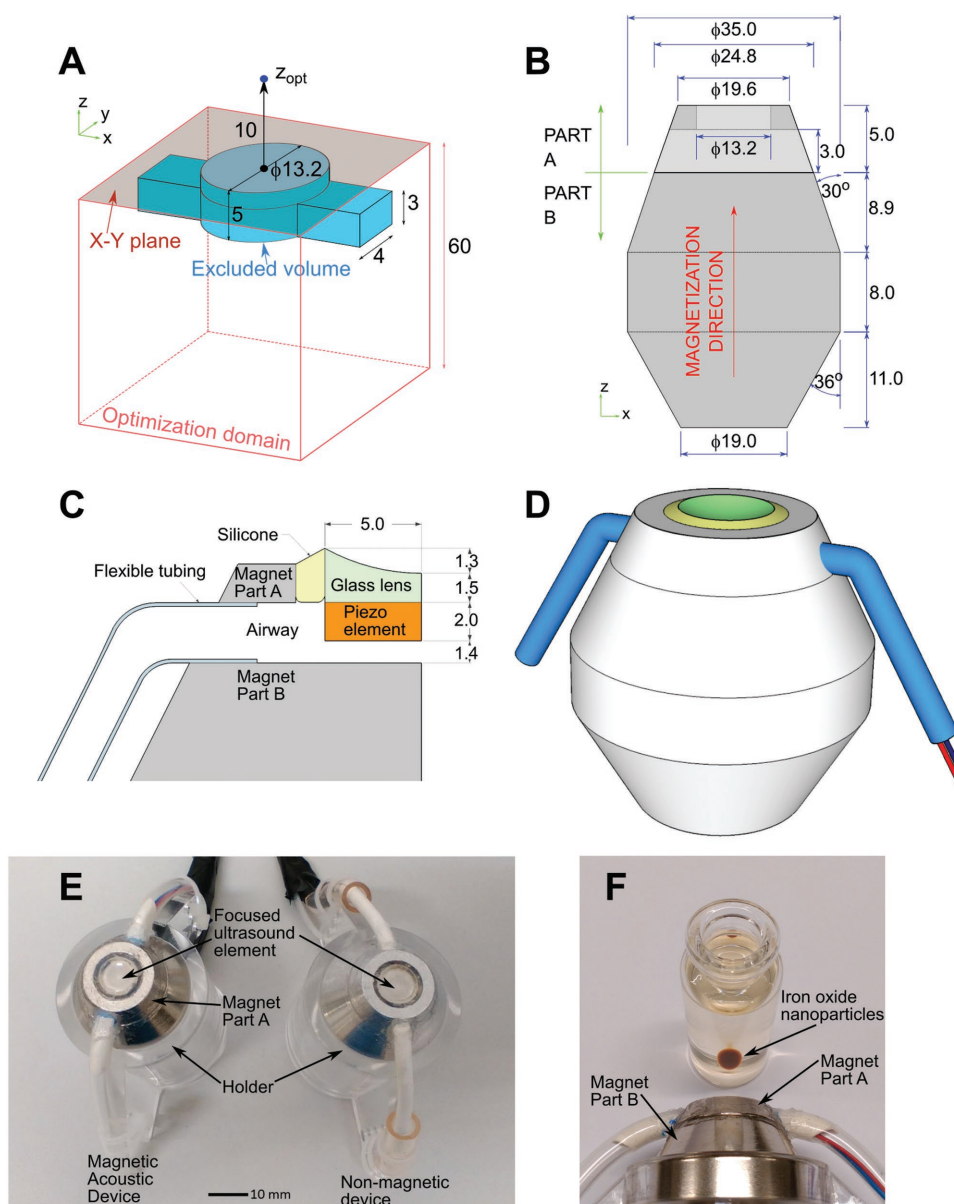
Figure 1. A) Schematic of the optimization domain used to generate a design for a magnet with uniform magnetization to apply magnetic force to a position of interest marked as z_{opt}. The light-red surface shows the x–y plane, and the origin is indicated by a black circle. The teal volume was excluded from the optimization to make space for an integrated ultrasound transducer and auxiliary components. B) Cross-section in the x–z plane of the magnet design based on the result of the optimization routine. The magnet was manufactured in two parts with parallel magnetization directions to self-assemble in only one stable configuration. C) Ultrasound element assembly showing piezoelectric disk and glass lens. D) Magnetic-acoustic device (MAD) assembly. E) Side by side photograph of the MAD and the nonmagnetic device manufactured for control measurements. F) Photograph illustrating how the MAD is capable of actuating and accumulating a suspension of iron oxide nanoparticles. All dimensions in mm.

concentrate and stimulate magnetic microbubbles. The magnetic component has been optimized using our previously reported algorithm to deliver the maximal magnetic force to a predefined region.[28] The ultrasonic component has been shaped to apply a focused acoustic field over the same region. The device reported here has been designed for length scales relevant to preclinical animal models as a proof of concept. Designs for clinically relevant tissue depths are discussed later.

2. Results

2.1. Finalized Design

A schematic of the combined MAD is shown in **Figure 1**. The magnetic field is produced by a uniformly magnetized volume of magnetic material. The shape of the magnet was determined using our previously described optimization routine,[28] employed in order to generate the optimal magnetic force at
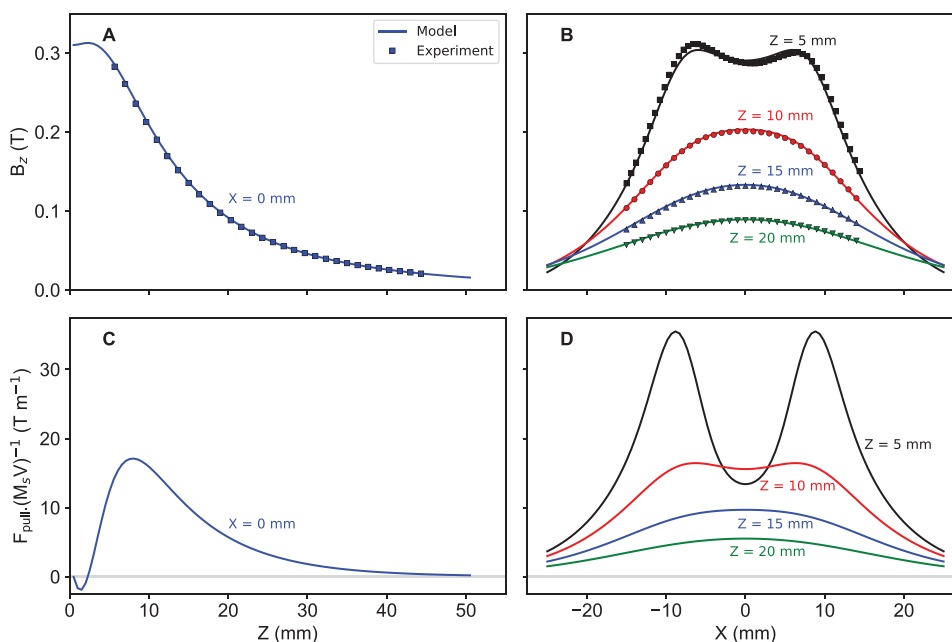
Figure 2. Field profiles along the A) z-axis and B) x-axis at various depths, z away from the face of the magnet. The z-component of the field was measured using a Hall probe (symbols) and compared with simulation (lines). Predictions for the normalized pull force are shown in C) along the z-axis and D) parallel to the x-axis at different z positions.

a position of interest (z_{opt}), in this case 10 mm from the face of the device. The optimization domain is shown in Figure 1A within a red cubic frame, along with a teal volume that was excluded from the optimization to make space for the components required to generate the acoustic field. The shape of the magnet design that resulted from the optimization routine is shown in Figure 1B. A single magnetization direction was utilized (in contrast to a Halbach array with multiple magnetization directions[29]) to simplify the assembly process. The magnet consisted of two parts made from N52 grade NdFeB permanent magnet material designed so that they would only self-assemble in one stable configuration due to dipole interactions. An aluminum copy was constructed with identical dimensions to be used as a nonmagnetic control device during testing.

The primary design goals for the ultrasound element were to provide a focused pressure field that spatially overlapped with the magnetic field peak, and to do so with sufficient amplitude to cause inertial cavitation of candidate microbubble formulations (this cavitation regime has been associated with desirable therapeutic effects[24,26]). After evaluation of candidate element designs using time domain finite element code (described in Section 5), a final configuration was chosen, featuring a 10 mm diameter piezoelectric disk with 1 MHz resonant frequency, fixed to a planoconcave glass lens to provide pressure field focusing (Figure 1C). A schematic of the complete device is shown in Figure 1D, in which the rectangular openings in the magnet were fitted with flexible tubing to allow airflow for passive cooling around the acoustic element and to provide a waterproof path for the element drive wires. Effort was made to minimize thermal coupling between the magnetic material and the ultrasound transducer while active. Temperature measurements made during operation with the drive parameters given

in Section 5 showed a temperature rise of just 1.3 °C at the upper magnet surface over a 20 min drive period. Photographs of the prototype MAD, its nonmagnetic replica, and an example of suspended iron oxide nanoparticle retention are shown in Figure 1E,F.

2.2. Calibration

Hall probe measurements of the z-component of the external field, B_z generated by the MAD are shown in **Figure 2**A,B, and showed good agreement with model predictions for its shape, particularly along the z-axis. Predictions for the normalized pull force (i.e., $F_{pull} = \mathbf{F} \cdot (-\mathbf{k})$, the component of the normalized force that points toward the magnet) are given in Figure 2C,D. Typically, the force from a solid magnetic volume decays almost exponentially with distance,[8] but the recess in the front face of the magnet compromises the magnetic force at short range, and even produces a small on-axis push force ($F_{pull} < 0$) within 2 mm of the magnet. It should be noted that the position along the axis where the pull force crosses to zero coincides with a saddle point in the field profile, and a local maximum in the magnetic potential energy ($U = -V\mathbf{M} \cdot \mathbf{B}$), as no arrangement of static permanent magnets can produce a stable potential energy well at range (i.e., Earnshaw's principle[8,30]). The normalized force (or force per moment) at the position of interest, z_{opt} is 15.8 T m^{-1}, which compares well with the force expected from a magnet optimized for the same parameters without the excluded volume (about 18 T m^{-1}[28]). At a distance of 10 mm the field is 0.2 T, which is enough to magnetize 10 nm SPIONs to 90% of the saturation magnetization, while at z = 20 mm, the field of 0.1 T can magnetize particles to 80% of saturation.[31]
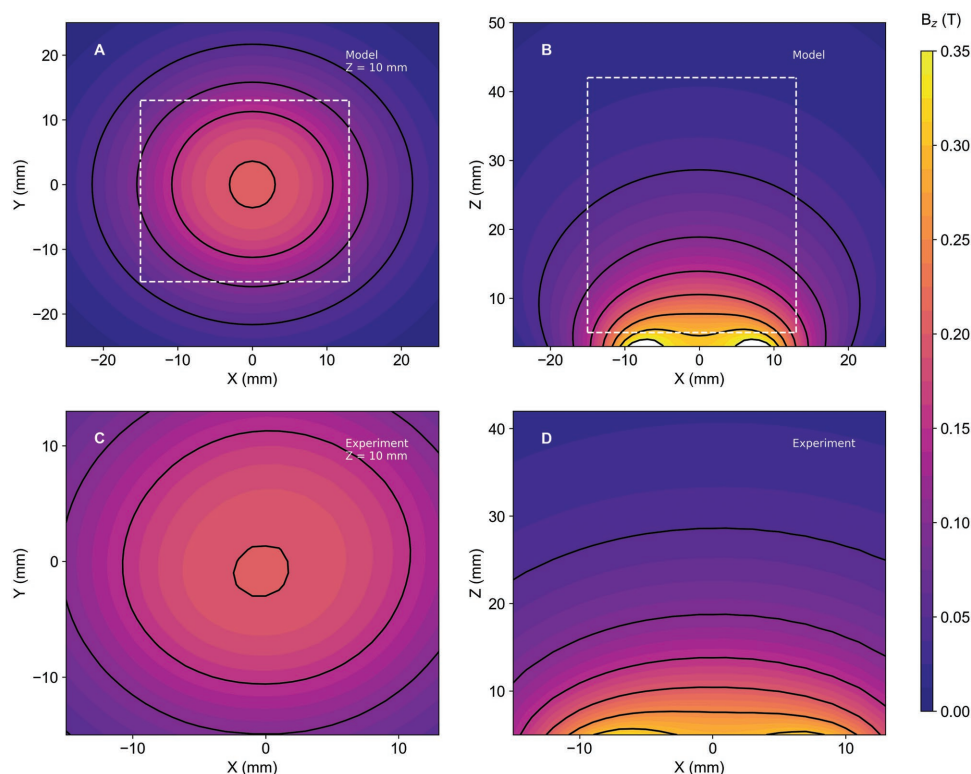
**ADVANCED
SCIENCE NEWS**

www.advancedsciencenews.com

**ADVANCED
MATERIALS
TECHNOLOGIES**

www.advmattechnol.de

Figure 3. Maps of the z-component of B simulated in the A) x–y plane at a range 10 mm above the surface of the MAD and B) in the x–z plane. Hall probe measurements of subsets of the same planes are respectively shown in (C) and (D). The dashed white boxes in (A) and (B) correspond to the range of the experimental measurements in (C) and (D).

The compromise in performance at short range can be understood by examining the profiles in Figure 2D. At z = 5 mm, the MAD emits strong forces at the edges of the device and a weaker central force. This type of force profile typically results in more particles accumulating closer to the edge of the magnet, rather than above the center,[32] resulting in an inefficient accumulation distribution if the target is aligned coaxially with the MAD. Our previous simulation results suggest that force profiles that rapidly vary and peak in a confined spatial region lead to more efficient accumulation of carriers to a coaxially aligned target.[32] The MAD emits this type of force profile beyond z = 15 mm, but at this range, the full-width half-maximum

(FWHM) of the profile is ≈40 mm. The implications of this are discussed further below.

Figure 3 shows that Hall probe measurements of the field emitted by the MAD agreed with simulations for the same planes. At a range of 10 mm from the surface of the array, simulations predicted a field of 0.203 T at the center of the x–y plane (Figure 3A), compared with a measured field of 0.201 T (Figure 3C).

Figure 4 shows the measured acoustic field profiles for the MAD ultrasound element at a frequency of 1.06 MHz, which was found to have the highest transmitting voltage response (TVR) in the 0.8–1.2 MHz data analysis band. The location of the focus was as designed (10 mm from the transducer surface), with a
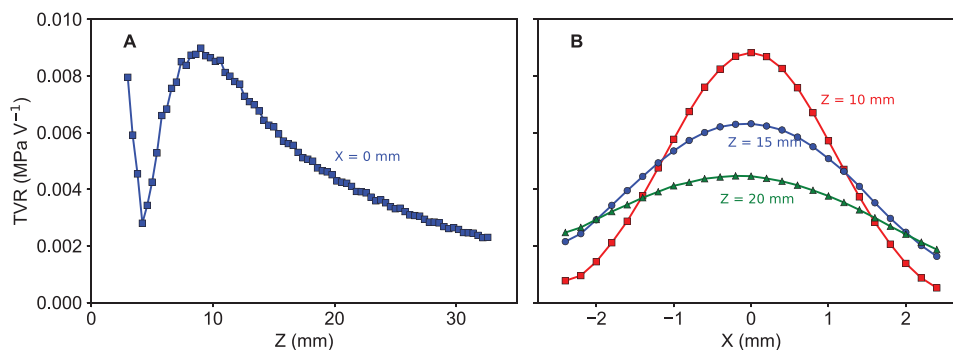

Figure 4. Transmitting voltage response profiles at 1.06 MHz A) on-axis and B) radially for three depths.

**ADVANCED
SCIENCE NEWS**
www.advancedsciencenews.com

**ADVANCED
MATERIALS
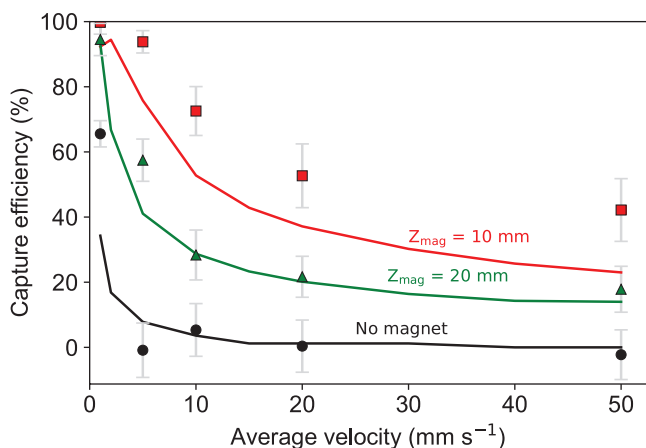TECHNOLOGIES**
www.advmattechnol.de

Figure 5. The capture efficiency measured by flowing microbeads at different mean fluid velocities with the channel set 10 and 20 mm away from the MAD. The lines show predicted values for the capture efficiency using the model from ref. [32]. The "no magnet" case (black line) is taken as the proportion of particles yet to reach the outlet after a simulation time of 2 min.

gradual attenuation and broadening of the beam pattern with increasing postfocal depth. Calibration of the nonmagnetic (aluminum body) device showed essentially identical frequency and field profiles to those shown in Figure 4, but with a modest global amplitude offset. This information was used to set drive voltage levels in subsequent retention and activation experiments, so that the output pressures would be the same for both devices.

2.3. Magnetic Capture Efficiencies

The ability of the MAD to magnetically target microscopic carriers was characterized by measuring the proportion of magnetic microbeads that were captured inside a flow phantom at different distances from the magnet, and over a range of mean flow velocities (**Figure 5**). The results were compared with predictions made using the numerical particle tracing simulations described in section 5, which were performed using effective particle parameters to match the magnetic properties measured

for the microbeads. A slightly higher capture efficiency than predicted was observed for most conditions, which was most likely due to interparticle interactions between the magnetized beads (interactions were ignored in the simulations for simplicity). Any offset in the magnet position with respect to the channel would also contribute to the discrepancy. However, both the measured and simulated capture efficiency values demonstrated that the MAD was capable of capturing more than 10% of the injected particles for all of the physiologically relevant flow velocities tested.

In the "no magnet" case for low velocities (1 mm s^{-1}) a relatively high "capture efficiency" (or, more accurately, a high proportion of unaccounted particles, as there was no external force to capture microbeads) was observed, as sampling was performed ≈1 min after injecting the particles. Simulations suggested this was an insufficient time period for the concentration to equilibrate at the outlet of the phantom at these fluid velocities. In effect, the very high discrepancy between the inlet and the outlet concentration observed for the 1 mm s^{-1} case is probably because, over the course of the measurement, there was insufficient time for particles to leave the channel. For higher velocities, the capture efficiencies decay for all magnet configurations, but increased magnetic force always results in enhanced capture.

2.4. Cavitation Activity of Captured Magnetic Microbubbles

Figure 6 shows examples of PCD responses during magnetic microbubble (MMB) retention and activation experiments. The average fluid velocity in the channel was 4.2 mm s^{-1} in these specific experiments. In the presence of MMBs, the PCD frequency spectrum elevates above the MMB-free background measurement in both tonal and broadband levels (Figure 6A), indicating a mix of bubble behaviors (including inertial cavitation) for the incident field level used. The lack of ultraharmonics (half-integer harmonics of the 1.06 MHz drive frequency) suggests the absence of stably cavitating bubbles. Although the results in Figure 6A are for single acquisitions, they are representative of the ensemble of collected data. The elevated 2–3 MHz background in the absence of MMBs is
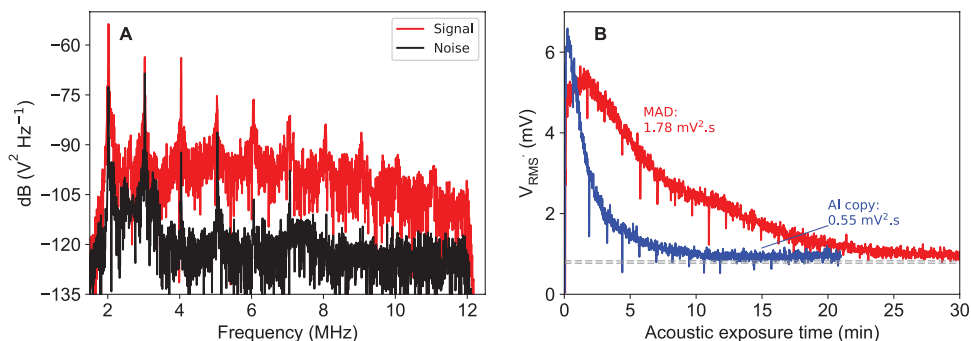

Figure 6. PCD data from MMB flow phantom experiments. A) Spectral densities of a signal taken with the MAD activating retained MMBs (signal) and a channel flushed with water (noise). B) RMS PCD voltage as a function of time after start of acoustic exposure. The horizontal dashed black lines indicate ±1 standard deviation of the background noise. Cumulative PCD energy values were calculated over the measurement time and displayed with units in mV^2 s. The transducer was operated with the following parameters: 1.06 MHz drive frequency, 0.5 MPa peak rarefaction pressure, 100 cycles per pulse and 1 s^{-1} pulse repetition frequency.
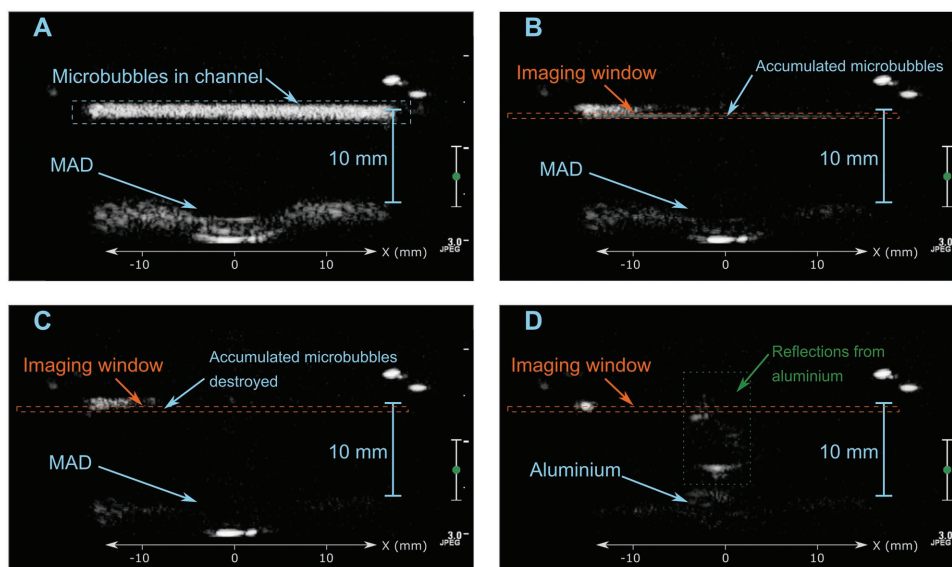
Figure 7. B-mode ultrasound images of magnetic microbubbles inside an agar flow phantom in the vicinity of the magnetic-acoustic device. A) Microbubbles were injected into a steady flow (4.2 mm s^{-1}) inside the channel. B) A retained bolus of accumulated microbubbles was observed and the corresponding change in intensity inside the imaging window (orange) measured. C) To verify that the accumulated particles were microbubbles, a short "flash" of high intensity ultrasound was applied, destroying the microbubbles. Images in (A)–(C) are from the same video, while D) is from a video recorded with the nonmagnetic copy in place of the MAD. Elevated reflections in (D) were caused by a slight difference in B-mode probe angle for the MAD and aluminum experiments.

caused primarily by scattering from the flow phantom internal and external boundaries, with secondary contributions from naturally occurring bubbles remaining in the filtered water. The temporal histories of PCD signals recorded with the magnetic and nonmagnetic devices are shown in Figure 6B. After exhibiting similar initial levels, the signals diverged strongly, with the magnetic (MAD) device sustaining MMB responses for a period more than four times longer compared to the nonmagnetic copy. The amount of time taken for the magnetically retained MMB response to decay to half of its peak value (relative to the noise floor) was 322 ± 52 s, compared with 74 ± 13 s using the nonmagnetic device. The cumulative signal energies (displayed in Figure 6B with units in mV^2 s) were calculated over the time interval for which the root mean square (RMS) PCD signals were more than twice that of the background. Magnetic retention enhanced the energy of the acoustic emissions by a factor of 3.3. As above, multiple studies have shown that both energy and duration of cavitation are positively correlated with therapeutic effect.[25,26,33]

2.5. Ultrasound Imaging of Captured MMBs

In order to demonstrate that the MAD could capture and accumulate carriers that are responsive to both acoustic and magnetic stimulation, B-mode ultrasound imaging was used to visualize microbubbles injected into an agar flow phantom. **Figure 7**B shows an example of the increased image intensity at the bottom of the channel due to accumulated microbubbles 4 min after the initial injection. Figure 7C shows that, after exposing the channel to a short, high intensity ultrasound "flash," these microbubbles were no longer visible confirming

that the change in image intensity was due to captured microbubbles. It was also noted that a brown residue of magnetic particles could still be seen in the vicinity of the magnet upon visual inspection of the flow phantom.

Figure 8 shows the change in image intensity produced by microbubble accumulation along the bottom of the channel. These data were compared with predictions for the accumulation of captured particles made using the model described in section 5 after normalization to the peak accumulation distribution (as the normalized accumulation distribution is mostly independent of the fluid velocity[32]). The model predicted that the greatest accumulation of particles would be observed in a
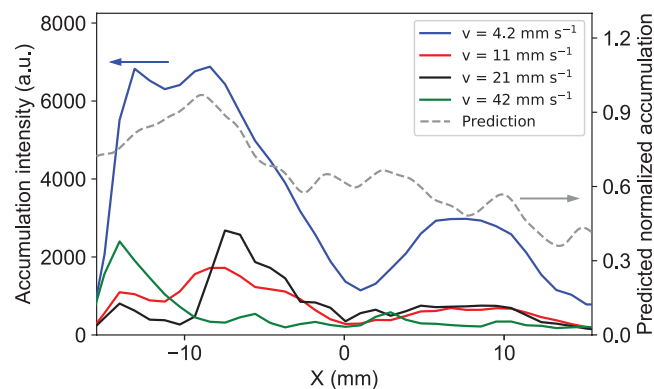

Figure 8. Ultrasound intensity profiles along the bottom of the channel shortly after starting B-mode imaging due to microbubbles captured by the MAD, with the mean fluid velocity inside the channel varied between 4.2 and 42 mm s^{-1} (left axis). The dashed line is a prediction of the relative linear density of captured particles, calculated using the model described in section 5, and normalized to the peak accumulation distribution (right axis).
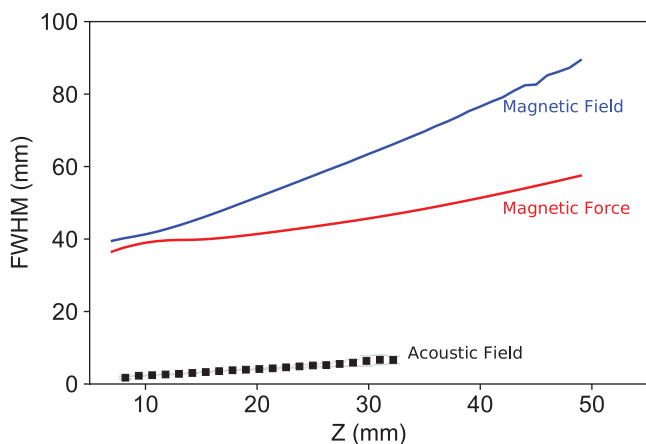
ADVANCED
SCIENCE NEWS
www.advancedsciencenews.com

ADVANCED
MATERIALS
TECHNOLOGIES
www.advmattechnol.de

Figure 9. Full-width half-maximum (FWHM) of the experimental acoustic field, and the simulated magnitude of the magnetic field and force parallel to the x-axis at different positions of z.

region ≈8 mm upstream from the center of the magnet, and qualitatively comparable behavior was seen for the intensity profiles, except at the highest flow velocity.

3. Discussion

Our previous work has indicated that the accumulation of magnetic particles in vitro and in vivo strongly depends on the force profile of the magnet[32] and this is further supported by the results of the present study. For the MAD design described here, the total magnetic force from the magnet was optimized at the target depth, but no subsequent attempt was made to tailor the force profile. The FWHM for each of the applied fields was determined from profiles parallel to the x-axis at different positions for z (**Figure 9**). As the FWHM of the applied acoustic field is relatively narrow compared with that of the magnet, the proportion of captured particles that are acoustically activated can be improved. This will be addressed in future designs. The optimal activation volume will depend upon the specific application. A small activation volume is advantageous for treatments in which the target is well defined, e.g., a detectable solid tumor or blood clot. A broader activation volume could be preferable in concert with applications that require additional biological targeting to locate diseased regions.[34–36]

The same approach could be used to design a device suitable for the larger length scales relevant for human applications. We have previously shown that, although the force from optimized magnet designs typically decays exponentially with distance, a Halbach array with a volume of 1000 cm³ would be capable of generating a field of 0.1 T and a normalized force of ≈4 T m^{-1} at a range of 50 mm.[28] To first order, this would be sufficient for 10% capture efficiency of magnetic microbubbles in vessels of ≈1 mm diameter with mean blood flow velocities up to 60 mm s^{-1}.[32] For clinical applications in cancer drug delivery, for example, higher capture efficiencies should be realizable as vessel diameters and flow rates are typically much smaller in tumor capillary systems.[37] A larger magnet volume would also provide more freedom to tailor both the magnetic and the acoustic field profiles to result in a more optimal distribution

of captured particles around the focus of the ultrasound transducer, particularly if the magnet could accommodate multiple ultrasound elements. Development of a portable, integrated device for applying acoustic and magnetic stimulus on human relevant length scales is the focus of our ongoing work.

The cavitation measurements show substantially more activity over a longer time scale when using magnetic targeting, which supports the results of previous in vitro[19] and in vivo studies[27] of cavitation from magnetically responsive microbubbles. As an example, Crake et al.[19] observed a factor of ≈2.5 increase in cumulative source energy monitored from magnetically captured microbubbles compared with no magnetic force, at flow conditions comparable to the current experiments. They made no attempt to optimize their magnet design in their study. By comparison, our combined design resulted in 3.3 times the total observed acoustic energy, with the magnet slightly further away from the target, and approximately an order of magnitude lower concentration of injected microbubbles. This is of interest due to intense active research into using cavitation nuclei for applications in drug delivery,[17,38,39] particularly with regards to using the mechanical action of cavitation to extravasate particles into solid tumors.[40,41] Further, ultrasonically induced cavitation of or in close proximity to drug carriers enables controlled drug release in a site-specific manner.[16,42] All of these effects can potentially be enhanced by the increased local concentration that MDT has been shown to provide for magnetically-responsive therapeutic carriers.[43–45]

The use of ultrasound-responsive magnetic carriers also addresses another challenge associated with MDT, that of imaging magnetic particles during therapy.[10] Magnet carrier formulations that use iron oxide nanoparticles are seen as favorable because iron oxide generates negative contrast in magnetic resonance imaging (MRI).[46,47] However, many of the systems proposed for magnetic targeting are incompatible with MRI instruments for safety reasons,[11] and magnetic delivery using MRI gradient coils can be challenging,[48,49] as conventional coils are not designed to generate sufficient magnetic force to capture SPIONs at particularly high flow regimes, such as those present in arteries. When MRI is incorporated with MDT studies, it is often used as a diagnostic tool after therapy.[50] Ultrasound, on the other hand, does not interact with external magnetic field sources,[51] and is also often less expensive than MRI, making it appropriate for portable or benchtop applications. Microbubbles have been used clinically for decades as ultrasound contrast agents.[13] In recent work they have been investigated as drug delivery carriers[16] and for magnetic drug targeting.[52–54] An integrated drug delivery device for simultaneously localizing and activating carriers that rely on acoustic and magnetic modalities would be highly advantageous for these types of applications. While our present device does not have imaging capabilities, the single element ultrasound transducer could be replaced with an array of elements to facilitate imaging and/or cavitation mapping.

This first iteration of the MAD design had compact size and weight (easily hand-held) with minimal development cost (first prototype cost <£1000 including nonrecoverable engineering charges). Based on prior experiences,[27,39,55] compactness of the design should be especially useful for future small animal or shallow clinical evaluations of targeted drug delivery concepts,

**ADVANCED
SCIENCE NEWS**
www.advancedsciencenews.com

**ADVANCED
MATERIALS
TECHNOLOGIES**
www.advmattechnol.de

where handling and positioning of multiple devices for near-surface targets is both logistically challenging and likely to increase experimental uncertainties.

4. Conclusion

In summary, we have designed an extracorporeal device for simultaneously applying magnetic and acoustic fields to concentrate and activate drug-carrying particles. The characteristics of both the magnetic and acoustic fields were measured in vitro and were shown to be in good agreement with theoretical predictions.

For all tested flow velocities up to 50 mm s^{-1} and tissue depths up to 20 mm, the device was able to capture and retain more than 10% of injected magnetic particles, and resulted in an increased intensity of acoustic emissions and sustained cavitation activity from magnetic microbubbles in an agar flow phantom. We believe that the current prototype of the device may be useful for small animal experiments involving the use of magnetically and acoustically responsive particles. Ongoing design efforts are focused on a scaled-up device for length scales relevant to human applications.

5. Experimental Section

Design and Assembly: The shape of the magnet was generated by the previously described optimization routine. Full details may be found in ref. [28] but briefly, the optimization routine considers possible magnetic configurations of a 3D arrangement of elements positioned within an optimization domain, retaining the magnetic configurations that result in the maximal magnetic force at the position of interest. For the present design, the total magnet volume, V_{mag} was constrained to 20 cm^3, which was chosen along with the value of $z_{opt} = 10$ mm to correspond with geometric scales relevant for pre-clinical animal models. To make space for the components required to generate the acoustic field, a specified volume was excluded from the optimization domain (Figure 1A). The excluded volume consisted of a cylinder to accommodate a cylindrical piezoelectric transducer and a rectangular cross-section channel embedded within the magnet volume. The latter provided space for wiring to the transducer and airflow to allow cooling of the piezoelectric element.

The finalized magnet configuration was manufactured as a bespoke design consisting of two parts made from N52 grade NdFeB permanent magnet material (Bunting Magnetics Europe Ltd., Berkhamsted, UK) with parallel magnetization directions, so that they would only self-assemble in one stable configuration. The top part encapsulates the excluded volume, and contains a cylindrical recess and a rectangular cross-section channel along the diameter on the side opposite the face. The same features were manufactured into an aluminum copy device for use as a nonmagnetic control device during testing.

The ultrasound element was designed to provide a focused pressure field to correspond with the magnetic position of interest, with sufficient amplitude to induce inertial cavitation in the microbubble formulation described below. The critical constraint on the design was to keep the element sufficiently compact so that the excluded magnet volume (and corresponding compromise to the magnetic field) would be minimized. Candidate element designs were evaluated using a time domain finite element code (PZFlex, Weidlinger Associates, Glasgow, UK) employing an axisymmetric geometry. The final configuration, chosen on the basis of predicted pressure field shape and estimated component cost, featured a 10 mm diameter piezoelectric disk with 1 MHz resonant frequency and wraparound electrodes (Noliac, Kvistgaard, Denmark).

The 1 MHz operating frequency was chosen as a compromise between the modest range of attenuation values in biological soft tissues[56] and the ability to produce suitable pressure amplitudes with a compact element. Pressure field focusing was provided by a planoconcave BK-7 glass lens (GalvOptics, Essex, UK) with 10.3 mm radius of curvature. A BK-7 glass formulation was chosen to enhance acoustic impedance matching between the piezoceramic and the external acoustic environment (water or soft biological tissue). The lens was fixed to one side of the piezoelectric disk using an epoxy (Araldite Ultra, Huntsman Advanced Materials, Everberg, UK) that was degassed for 1 min after mixing and cured according to manufacturer directions.

To assemble the MAD, first the two magnet components were combined, with care taken to avoid damaging the nickel coating. Next, the acoustic element was centered 1.4 mm above the bottom of the excluded magnet volume using nonferrous spacer rods, after which the perimeter gap between the acoustic element and magnet was sealed using silicone (Loctite SI 4145, Henkel Ltd., Hemel Hempstead, UK). Two additional applications of sealant were applied after the first had dried and the spacer rods were removed. Flexible tubing was attached to the rectangular openings of the magnet and a final application of silicone was used to seal the tubing entry points and the two magnet sections.

A number of considerations constrained the design process. N52 grade NdFeB was chosen for the magnet material due to it having one of the highest magnetization values of commercial NdFeB grades 1.02 × 10^6 A m^{-1}), and a temperature rating of about 80 °C[57] (i.e., well above any physiologically relevant temperatures). Using a grade of NdFeB with a high remanent magnetization has a number of advantages over alternative magnetic systems, such as electromagnets:[58] as the magnetic energy is stored internally, no external power supply is required, meaning the device can be small and light-weight, and passive cooling is only required to keep the material below the rated temperature.[59] Thermal testing was performed using a series of fine needle thermocouples (Hypo 33-1-T, Omega, Stamford, CT, USA) to probe different positions on the MAD during operation of the transducer (1 MHz, 3000 cycle tone pulses with 75 V amplitude driving voltage and 30% duty cycle).

Calibration of Applied Fields: The magnetic field and forces generated by the MAD at specified positions outside of the magnet were predicted using a model previously described and experimentally verified[60] in which the magnet was broken into a 3D lattice of evenly distributed point moments, and the field calculated by summing the contributed dipole field from each moment. The model also predicted the magnetic force due to the field gradient

$$F_M(r) = MV \cdot \nabla(B(r)) \tag{1}$$

expressed as a "normalized force" or force per moment, which is used here for convenience because it has the same units as the field gradient (T m^{-1}):

$$F_M/(M_sV) = (M/M_s)|\nabla(B)| \tag{2}$$

Here, F_M is the magnitude of the magnetic force, M is the magnetization, V is the volume of the superparamagnetic particle, M_s is the saturation magnetization of the particle, and B is the magnitude of the magnetic field, $B(r) = (B_x, B_y, B_z)$ at a position r.

Measurements of the vector field generated by the magnet were performed using a three-axis Hall probe connected to a Model 460 3-Channel Gaussmeter (Lake Shore Cryotronics, Inc., OH, USA). The probe was mounted on a set of three MTS Series Motorized Translation Stages (Thorlabs, Inc., NJ, USA) with travel ranges of 50 mm, configured to give controllable translation in each of three orthogonal directions.

Acoustic pressure field profiles were measured with a needle hydrophone (200 μm diameter needle, Precision Acoustics, Dorchester, UK) while the MAD front face was submerged in a tank filled with filtered and degassed water. The ultrasound element was driven with a three cycle, 1 MHz tone burst from a waveform generator (33250, Agilent

1800081 (8 of 11)

Technologies, Cheshire, UK) and amplified with a nominal gain of 55 dB (1040L, E&I Ltd., Rochester, NY, USA). Automated scan control software (UMS2, Precision Acoustics, Dorchester, UK) incrementally translated the hydrophone beneath the stationary MAD and transferred its response signals from an oscilloscope (Waverunner 64Xi, Teledyne LeCroy, Geneva, Switzerland) to computer disk for analysis. Drive voltage (PP007-WR, LeCroy) and current (4100, Pearson Electronics, Palo Alto, CA, USA) probes were monitored to ensure proper system operation and allow subsequent calculation of electrical impedance. Calibration data sets were processed in MATLAB (The MathWorks Inc., Natick, MA, USA) using the following steps: i) application of a high pass filter to remove any DC offset in the data traces, ii) calculation of hydrophone $A(f,x,y,z)$ and drive voltage $V(f)$ Fourier transforms, and iii) calculation of the TVR at each frequency and scan grid point (x,y,z): $TVR(f,x,y,z) = A(f,x,y,z)/(V(f)S(f))$ where $S(f)$ is the hydrophone sensitivity. Water temperature was monitored with a glass thermometer, with values used to calculate sound speed[61] for use in estimating hydrophone position along the MAD symmetry axis.

Magnetic Microbead Retention Experiments: Magnetic retention experiments were performed to demonstrate the effectiveness of the MAD for retaining magnetic carriers against flow. Polystyrene magnetic microbeads ($(2.0–2.9) \times 10^{-6}$ m diameter, Spherotech, Inc., Lake Forest, IL, USA) were used as model magnetic carriers, due to their relatively low size dispersity and uniform magnetic characteristics. The mean size of the microbeads was comparable to that of the magnetic microbubbles described below. Their magnetic response was characterized using an MPMS superconducting quantum interference device (SQUID) magnetometer (Quantum Design, Inc., San Diego, CA, USA) as reported previously,[32] which indicated an effective, superparamagnetic cluster size of 8.6 nm and a 16.2% weight loading of iron oxide in polystyrene. As the dispersity of the particles was fairly low, the magnetic properties of all particles in the ensemble could be reasonably approximated by using just these effective parameters (such an approximation would not be appropriate with magnetic microbubbles because the particle-to-particle variation was too large). The microbeads were diluted to a concentration of 4×10^6 mL^{-1} and injected into a straight, cylindrical channel (1.2 mm inner diameter) embedded in a flow phantom, using a syringe pump (NE-1000, New Era Pump Systems, Inc., Farmingdale, NY, USA). The phantom consisted of a degassed mixture of 2.5% agar (UltraPure Agarose 1000, Life Technologies, Paisley, UK) and filtered water poured into a thin rectangular mould bounded by 0.015 mm thick mylar sheets (PMX980, HiFi, Hertfordshire, UK) to allow uninhibited acoustic transmission. The phantom frame, fasteners, and flow channel conduits were all made of nonferrous polymer materials to avoid extraneous stray magnetic fields during the tests. The MAD was affixed to the outside of the phantom frame using a 3D printed guiding ring, so that the relative position of the MAD to the flow phantom could be reproducibly set between experimental runs. The MAD was positioned so that there was a distance of either 10 or 20 mm from the face of the magnet to the channel axis. The average fluid velocity in the flow channel was varied between 1 and 50 mm s^{-1} (a range of flow velocities seen in intratumoral blood flow[62]), corresponding to a Reynolds number range of 1.35 to 67.4.

The capture efficiency was determined by comparing the concentration of microbeads before (initial, C_i) and after (final, C_f) the flow phantom. To measure the concentration, a modified procedure adapted from ref. [63] was used, whereby a series of 2D images were obtained of sampled microbeads using a 40× objective lens on a Leica DM500 optical microscope with an integrated CCD camera (Larch House, Milton Keynes, UK), and analyzed with a custom image processing routine based on the NumPy package for Python 3.5. The microbead concentration prior to the flow phantom was used as a reference for the concentration (per unit volume). The capture efficiency was calculated as

$$C.E. = (C_i - C_f)/C_i \times 100\% \qquad (3)$$

The experiments were repeated using the nonmagnetic aluminum copy of the MAD.

Predictions of the capture efficiency were made using a numerical model for particle trajectories reported previously.[32] In summary, simulations were performed of an ensemble of particles with the same magnetic properties as the microbeads, which were distributed evenly at the inlet of a channel carrying laminar flow. A force balance was used to determine the particle trajectories and calculate the proportion of particles that were captured by the magnet and the proportion that reached the outlet. The model parameters were selected to match the experimental conditions and the simulations were run until all particles reached their final position. The simulations were repeated without an external magnetic force over 2 min of simulation time only, as all magnet simulations had all particles reach their final positions within 2 min of simulation time. As the aim of the study was to determine differences in capture efficiency for different conditions, water was used as the suspending fluid for both the simulations and the experiments rather than blood.

Magnetic Microbubble Acoustic Intensity Experiments: Magnetic microbubbles were prepared following an slightly modified version of the method developed by Stride et al.:[5] 1,2-distearoyl-sn-glycero-3-phosphocholine (DSPC) was purchased from Avanti Polar Lipids, Inc. (Alabaster, AL, USA). Polyoxyethylene (40) stearate (PEG40S), chloroform, and Dulbecco's phosphate-buffered saline were purchased from Sigma-Aldrich Ltd. (Gillingham, Dorset, UK). Isoparaffin coated magnetic nanoparticles (10 nm diameter) were purchased from Liquids Research (Bangor, UK). Sulfur hexafluoride (SF$_6$) was purchased from The BOC Group (Guilford, Surrey, UK). A mixture of DSPC:PEG40S in chloroform (9:1 molar ratio) was prepared by adding 621 µL of DSPC (25 mg mL^{-1}) and 447 µL of PEG40S (10 mg mL^{-1}) into a glass vial. The sample was covered with pierced parafilm and heated to 50 °C overnight to evaporate the solvent.

After complete solvent evaporation, the dried lipid film was suspended in 5 mL of PBS for 1 h at 75 °C under constant magnetic stirring. The stir bar was removed from the sample and the solution was sonicated using a XL2000 ultrasonic cell disruptor from Misonix, Inc. (Farmingdale, NY, USA). The sonicator was used at power setting 4 (8 W$_{RMS}$ output power) for 15 s with a 3 mm diameter tip, operating at 22.5 kHz, with the probe tip held within the solution. This was immediately followed by sonication at the gas–water interface with the probe tip touching the liquid surface, under positive pressure of SF$_6$ and at power setting 19 (38 W$_{RMS}$) for 10 s. 15 µL of isoparaffin coated iron oxide nanoparticles (10 nm diameter) was then added to the mixture and the vial was gently swirled for 10 s. The solution was again sonicated with the probe tip held within the liquid at power setting 4 for 15 s, followed by cooling of the sample at 5 °C for 15 min. Then, the solution was again sonicated at the gas–water interface, under positive pressure of SF$_6$ at power setting 19 (38 W$_{RMS}$) for 10 s. Finally, the magnetic microbubble solution was capped and placed on ice for 10 min before further analysis.

Microbubbles were observed using a Leica DM500 optical microscope (Larch House, Milton Keynes, UK) with a 40× objective lens, and a Neubauer haemocytometer from Hausser Scientific (Horsham, PA, USA). Microbubble concentration and size analysis was performed using a purposely written image analysis software in MATLAB.[63] On average ($n = 5$), each batch produced a suspension of $(4.4 \pm 0.6) \times 10^8$ magnetic microbubbles per mL with an average diameter of 2.6 ± 0.25 µm.

In order to demonstrate that the MAD could capture acoustically responsive magnetic carriers, microbubbles were diluted to 1/10 of the batch concentration and injected into a steady laminar fluid flow, established inside the agar flow phantom described above. The magnet was fixed to the phantom holder at a distance of 10 mm from the channel, as described above, and the average fluid flow velocity was varied between 4 and 42 mm s^{-1}. After waiting for 4 min (which, according to simulations, was sufficiently long for a captured bolus of magnetic microbubbles to form inside the channel near the magnet), the channel was imaged using a commercially available ultrasound system (iU22, Philips, Bothell, WA, USA) with a linear array (L12-5, Philips) angled ≈40° off the MAD symmetry axis. Videos consisting of B-mode images were recorded for 1 min at a frame rate of 13 frames s^{-1}.

1800081 (9 of 11)

An ultrasound drive level corresponding to a mechanical index (MI) value of 0.15 (comparable to conventional imaging conditions) was used to image the accumulated bolus. To minimize changes in intensity due to microbubble destruction, a series of frames in a 5 s window was selected for processing immediately after the retained bubbles had cleared from the imaging field of view. These images were analyzed using a custom image processing routine based on the NumPy package for Python 3.5. The bottom of the channel in the images was windowed, and the position dependent intensity, $I(x)$ was determined by taking a weighted local regression of the total intensity in the part of the window between $x \pm dx$, which was then averaged for all selected images from the same video. All experimental runs were repeated with the nonmagnetic control device (Figure 7D). The measured values of $I(x)$ were compared with numerical predictions for the accumulation distribution, which were calculated using the model reported previously and summarized above.[32] The accumulation distribution was defined as the proportion of captured particles with simulated final positions ranging between $x \pm dx$.

The combined magnetic retention and acoustic activation capabilities of the MAD were demonstrated by monitoring acoustic emissions from the flow channel while driving the ultrasonic element. The signal generation chain was the same as described in Section 5, Calibration of Applied Fields but the drive signal was lengthened to 100 cycles, and the pulse repetition period slowed to 1.0 s. The drive amplitude was set so that the peak rarefactional pressure at the center of the channel would be 0.50 MPa, based on the results of free field calibrations described in Section 5. Ultrasonic emissions from the channel were observed using a spherically focused single element transducer (7.5 MHz center frequency, 12.7 mm diameter, 75 mm focal distance, Olympus NDT, Essex, UK) operating as a passive cavitation detector (PCD). Signals from the PCD were preamplified (SR445A, SRS, Sunnyvale, CA, USA), digitized (Handyscope HS3, TiePie Engineering, Sneek, Netherlands) upon triggering from the waveform generator, and streamed to a computer disk.

Prior to conducting cavitation monitoring experiments, alignment of the PCD with the section of channel directly in front of the MAD was achieved by temporarily introducing an air pocket into the channel. The PCD was then connected to a pulser (5072PR, Olympus NDT), and its position adjusted to maximize the scattered signal amplitude within the expected propagation time window. For all experiments, the PCD was positioned so that there was an angle of ≈40° between its axis and that of the MAD element in order to minimize mutual scattering.

Conflict of Interest

The manuscript authors are also named inventors on a patent application relating to the device.

[1] P. K. Gupta, C. T. Hung, *Life Sci.* **1989**, *44*, 175.
[2] A. S. Lubbe, C. Bergemann, H. Riess, F. Schriever, P. Reichardt, K. Possinger, M. Matthias, B. Dorken, F. Herrmann, R. Gurtler, P. Hohenberger, N. Haas, R. Sohr, B. Sander, A. J. Lemke, D. Ohlendorf, W. Huhnt, D. Huhn, *Cancer Res.* **1996**, *56*, 4686.
[3] A. S. Lübbe, C. Bergemann, J. Brock, D. G. McClure, *J. Magn. Magn. Mater.* **1999**, *194*, 149.
[4] Q. A. Pankhurst, N. T. K. Thanh, S. K. Jones, J. Dobson, *J. Phys. D: Appl. Phys.* **2009**, *42*, 224001.
[5] E. Stride, C. Porter, A. G. Prieto, Q. Pankhurst, *Ultrasound Med. Biol.* **2009**, *35*, 861.
[6] P. Pouponneau, J.-C. Leroux, G. Soulez, L. Gaboury, S. Martel, *Biomaterials* **2011**, *32*, 3481.
[7] C. F. Driscoll, R. M. Morris, A. E. Senyei, K. J. Widder, G. S. Heller, *Microvasc. Res.* **1984**, *27*, 353.
[8] M. E. Hayden, U. O. Häfeli, *J. Phys.: Condens. Matter* **2006**, *18*, S2877.
[9] J. Owen, P. Grove, P. Rademeyer, E. Stride, *J. R. Soc., Interface* **2014**, *11*, 20140622.
[10] B. Shapiro, S. Kulkarni, A. Nacev, S. Muro, P. Y. Stepanov, I. N. Weinberg, *Wiley Interdiscip. Rev.: Nanomed. Nanobiotechnol.* **2015**, *7*, 446.
[11] J. F. Schenck, *J. Magn. Reson. Imaging* **2000**, *12*, 2.
[12] B. Gleich, J. Weizenecker, *Nature* **2005**, *435*, 1214.
[13] R. S. Meltzer, E. G. Tickner, T. P. Sahines, R. L. Popp, *J. Clin. Ultrasound* **1980**, *8*, 121.
[14] C. J. Harvey, J. M. Pilcher, R. J. Eckersley, M. J. K. Blomley, D. O. Cosgrove, *Clin. Radiol.* **2002**, *57*, 157.
[15] J. Hua, L. E. Erickson, T.-Y. Yiin, L. A. Glasgow, *Crit. Rev. Biotechnol.* **2008**, *13*, 305.
[16] I. Lentacker, S. C. De Smedt, N. N. Sanders, *Soft Matter* **2009**, *5*, 2161.
[17] C. C. Coussios, R. A. Roy, *Annu. Rev. Fluid Mech.* **2008**, *40*, 395.
[18] G. Guo, L. Lu, L. Yin, J. Tu, X. Guo, J. Wu, D. Xu, D. Zhang, *Phys. Med. Biol.* **2014**, *59*, 6729.
[19] C. Crake, M. d. S. Victor, J. Owen, C. Coviello, J. Collin, C.-C. Coussios, E. Stride, *Phys. Med. Biol.* **2015**, *60*, 785.
[20] X. Zhao, P. A. Quinto-Su, C.-D. Ohl, *Phys. Rev. Lett.* **2009**, *102*.
[21] D. Vlaskou, O. Mykhaylyk, F. Krötz, N. Hellwig, R. Renner, U. Schillinger, B. Gleich, A. Heidsieck, G. Schmitz, K. Hensel, C. Plank, *Adv. Funct. Mater.* **2010**, *20*, 3881.
[22] J. Owen, B. Zhou, P. Rademeyer, M.-X. Tang, Q. Pankhurst, R. Eckersley, E. Stride, *Theranostics* **2012**, *2*, 1127.
[23] Y. Heun, S. Hildebrand, A. Heidsieck, B. Gleich, M. Anton, J. Pircher, A. Ribeiro, O. Mykhaylyk, D. Eberbeck, D. Wenzel, A. Pfeifer, M. Woernle, F. Krötz, U. Pohl, H. Mannell, *Theranostics* **2017**, *7*, 295.
[24] N. McDannold, N. Vykhodtseva, K. Hynynen, *Phys. Med. Biol.* **2006**, *51*, 793.
[25] J. H. Hwang, J. Tu, A. A. Brayman, T. J. Matula, L. A. Crum, *Ultrasound Med. Biol.* **2006**, *32*, 1611.
[26] Y. Qiu, Y. Luo, Y. Zhang, W. Cui, D. Zhang, J. Wu, J. Zhang, J. Tu, *J. Controlled Release* **2010**, *145*, 40.
[27] C. Crake, J. Owen, S. Smart, C. Coviello, C.-C. Coussios, R. Carlisle, E. Stride, *Ultrasound Med. Biol.* **2016**, *42*, 3022.

[28] L. C. Barnsley, D. Carugo, E. Stride, *J. Phys. D: Appl. Phys.* **2016**, *49*, 225501.

[29] K. Halbach, *Nucl. Instrum. Methods* **1980**, *169*, 1.

[30] A. Nacev, I. N. Weinberg, P. Y. Stepanov, S. Kupfer, L. O. Mair, M. G. Urdaneta, M. Shimoji, S. T. Fricke, B. Shapiro, *Nano Lett.* **2014**, *15*, 359.

[31] M. Kettering, H. Zorn, S. Bremer-Streck, H. Oehring, M. Zeisberger, C. Bergemann, R. Hergt, K.-J. Halbhuber, W. A. Kaiser, I. Hilger, *Phys. Med. Biol.* **2009**, *54*, 5109.

[32] L. C. Barnsley, D. Carugo, M. Aron, E. Stride, *Phys. Med. Biol.* **2017**, *62*, 2333.

[33] Y. Zhou, J. Cui, C. X. Deng, *Biophys. J.* **2008**, *94*, L51.

[34] U. A. Gunasekera, Q. A. Pankhurst, M. Douek, *Targeted Oncol.* **2009**, *4*, 169.

[35] N. Schleich, C. Po, D. Jacobs, B. Ucakar, B. Gallez, F. Danhier, V. Préat, *J. Controlled Release* **2014**, *194*, 82.

[36] H.-L. Xu, K.-L. Mao, Y.-P. Huang, J.-J. Yang, J. Xu, P.-P. Chen, Z.-L. Fan, S. Zou, Z.-Z. Gao, J.-Y. Yin, J. Xiao, C.-T. Lu, B.-L. Zhang, Y.-Z. Zhao, *Nanoscale* **2016**, *8*, 14222.

[37] E. N. Marieb, K. N. Hoehn, *The Cardiovascular System: Blood Vessels, Human Anatomy, Physiology*, 9th ed.,Pearson, Glenview, USA **2013**.

[38] S. R. Sirsi, M. A. Borden, *Adv. Drug Delivery Rev.* **2014**, *72*, 3.

[39] J. Y. Lee, D. Carugo, C. Crake, J. Owen, M. de Saint Victor, A. Seth, C. Coussios, E. Stride, *Adv. Mater.* **2015**, *27*, 5484.

[40] B. Rifai, C. D. Arvanitis, M. Bazan-Peregrino, C.-C. Coussios, *J. Acoust. Soc. Am.* **2010**, *128*, EL310.

[41] J. J. Kwan, R. Myers, C. M. Coviello, S. M. Graham, A. R. Shah, E. Stride, R. C. Carlisle, C. C. Coussios, *Small* **2015**, *11*, 5305.

[42] K. Kooiman, M. R. Böhmer, M. Emmer, H. J. Vos, C. Chlon, W. T. Shi, C. S. Hall, S. H. P. M. de Winter, K. Schroën, M. Versluis, N. de Jong, A. van Wamel, *J. Controlled Release* **2009**, *133*, 109.

[43] A. S. Lübbe, C. Alexiou, C. Bergemann, *J. Surg. Res.* **2001**, *95*, 200.

[44] H. Nobuto, T. Sugita, T. Kubo, S. Shimose, Y. Yasunaga, T. Murakami, M. Ochi, *Int. J. Cancer* **2004**, *109*, 627.

[45] M. Muthana, A. J. Kennerley, R. Hughes, E. Fagnano, J. Richardson, M. Paul, C. Murdoch, F. Wright, C. Payne, M. F. Lythgoe, N. Farrow, J. Dobson, J. Conner, J. M. Wild, C. Lewis, *Nat. Commun.* **2015**, *6*, 8009.

[46] Q. A. Pankhurst, J. Connolly, S. K. Jones, J. Dobson, *J. Phys. D: Appl. Phys.* **2003**, *36*, R167.

[47] M. Das, D. Mishra, T. K. Maiti, A. Basak, P. Pramanik, *Nanotechnology* **2008**, *19*, 415101.

[48] J. B. Mathieu, G. Beaudoin, S. Martel, *IEEE Trans. Biomed. Eng.* **2006**, *53*, 292.

[49] S. Martel, J.-B. Mathieu, O. Felfoul, A. Chanu, E. Aboussouan, S. Tamaz, P. Pouponneau, L. H. Yahia, G. Beaudoin, G. Soulez, M. Mankiewicz, *Appl. Phys. Lett.* **2007**, *90*, 114105.

[50] B. Chertok, B. A. Moffat, A. E. David, F. Yu, C. Bergemann, B. D. Ross, V. C. Yang, *Biomaterials* **2008**, *29*, 487.

[51] K. Hynynen, *J. Magn. Reson. Imaging* **2011**, *34*, 482.

[52] K. Soetanto, H. Watarai, *Jpn. J. Appl. Phys.* **2000**, *39*, 3230.

[53] C. Plank, O. Zelphati, O. Mykhaylyk, *Adv. Drug Delivery Rev.* **2011**, *63*, 1300.

[54] J. Owen, P. Rademeyer, D. Chung, Q. Cheng, D. Holroyd, C. Coussios, P. Friend, Q. A. Pankhurst, E. Stride, *Interface Focus* **2015**, *5*, 20150001.

[55] Y. Sheng, E. Beguin, H. Nesbitt, S. Kamila, J. Owen, L. C. Barnsley, B. Callan, C. O'Kane, N. Nomikou, R. Hamoudi, M. A. Taylor, M. Love, P. Kelly, D. O'Rourke, E. Stride, A. P. McHale, J. F. Callan, *J. Controlled Release* **2017**, *262*, 192.

[56] F. A. Duck, *Physical Properties of Tissues: A Comprehensive Reference Book*, Academic Press, London **1990**.

[57] M. Haavisto, M. Paju, *IEEE Trans. Magn.* **2009**, *45*, 5277.

[58] C. Alexiou, D. Diehl, P. Henninger, H. Iro, R. Rockelein, W. Schmidt, H. Weber, *IEEE Trans. Appl. Supercond.* **2006**, *16*, 1527.

[59] O. Baun, P. Blümler, *J. Magn. Magn. Mater.* **2017**, *439*, 294.

[60] L. C. Barnsley, D. Carugo, J. Owen, E. Stride, *Phys. Med. Biol.* **2015**, *60*, 8303.

[61] W. Marczak, *J. Acoust. Soc. Am.* **1997**, *102*, 2776.

[62] K. Shimamoto, S. Sakuma, T. Ishigaki, N. Makino, *Radiology* **1987**, *165*, 683.

[63] C. A. Sennoga, V. Mahue, J. Loughran, J. Casey, J. M. Seddon, M. Tang, R. J. Eckersley, *Ultrasound Med. Biol.* **2010**, *36*, 2093.